HOKKAIDO UNIVERSITY

Title	Formation-structure-properties of niobium-oxide nanocolumn arrays via self-organized anodization of sputter-deposited aluminum-on-niobium layers
Author(s)	Mozalev, Alexander; Vazquez, Rosa M.; Bittencourt, Carla et al.
Citation	Journal of Materials Chemistry C, 2(24), 4847-4860 https://doi.org/10.1039/c4tc00349g
Issue Date	2015-04-03
Doc URL	https://hdl.handle.net/2115/58299
Type	journal article
File Information	Manuscript JMCC-revised and accepte.pdf

Hokkaido University Collection of Scholarly and Academic Papers : HUSCAP

Dynamic Article Links ►

J. Mater. Chem. C, 2014, X (XX), XXX-XXX

Full paper

Formation-structure-properties of niobium-oxide nanocolumn arrays via self-organized anodizing of sputter-deposited aluminum-on-niobium layers

Alexander Mozalev,[a] Rosa M. Vázquez,[b] Carla Bittencourt,[c] Damien Cossement,[d] Francesc Gispert-Guirado,[e] Eduard Llobet,[b] Hiroki Habazaki[f]

Received
DOI: 10.1039/b000000x

Nanostructured niobium oxide (NO) semiconductor is gaining increasing attention as electronic, optical, and electro-optic material. However, the preparation of stable NO nanofilms with reproducible morphology and behavior remains a challenge. Here we show a rapid, well-controlled, and efficient way to synthesize NO films with the self-organized columnlike nanostructured morphologies and advanced functional properties. The films are developed via the growth of a nanoporous anodic alumina layer, followed by the pore-directed anodizing of the Nb underlayer. The columns may grow 30-150 nm wide, up to 900 nm long, with the aspect ratio up to 20, being anchored to a thin continuous oxide layer that separates the columns from the substrate. The as anodized films have a graded chemical composition changing from amorphous Nb_2O_5 mixed with Al_2O_3, Si-, and P-containing species in the surface region to NbO_2 in the lower film layer. The post-anodizing treatments result in the controlled formation of Nb_2O_5, NbO_2, and NbO crystal phases, accompanied by transformation from nearly perfect dielectric to *n*-type semiconductor behavior of the films. The approach allows for the smooth film growth without early dielectric breakdown, stress-generated defects, or destructive dissolution at the respective interfaces, which is a unique situation in the oxide films on niobium. The functional properties of the NO films, revealed to date, allow for potential applications as nanocomposite capacitor dielectrics and active layers for semiconductor gas microsensors with the sensitivity to ethanol and the response to hydrogen being among best ever reported.

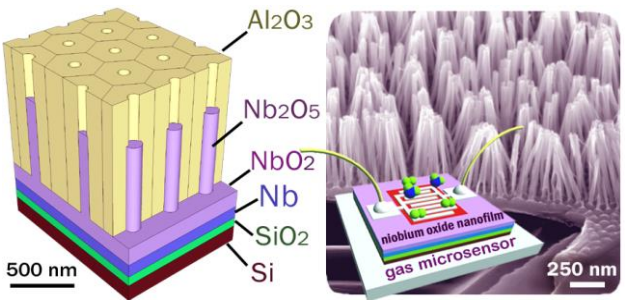

Introduction

Niobium oxide (NO) and NO-containing films have been proposed for a variety of applications, including semiconductor gas sensors, photoanodes, materials for catalysis, biocompatible coatings, energy storage, and electrochromic devices.[1-6] In the microelectronic industry, NO is considered as a high-permittivity dielectric instead for silicon dioxide in semiconductor devices.[7] NO is also described as a promising substitute for tantalum oxide in solid-electrolyte Ta_2O_5/Ta capacitors,[8] due to the advantage of greater natural abundance and lower price of raw material.

Despite the large number of potential applications and useful properties, the well-controlled preparation of NO films with the reproducible behavior remains a challenge. This is partly due to the existence of at least three stable NO's each having different electrical properties ranging from conducting NbO through semiconducting NbO_2 to insulating Nb_2O_5.[9] Additionally, in the Nb-O system there exist numerous metastable oxides NbO_x with $0 < x < 1$ and $2.0 < x < 2.5$ as well as a multitude of Nb_2O_5 polymorphic modifications. Nowadays, the functionality of NO for possible applications to optical and electronic devices has been investigated with regard to increasing the surface-to-volume ratio and making the films periodically structured.[10] Nanostructuring of NO offers unique opportunities for the development of NO-based materials with improved performances or substantially enhanced properties in some sense. Glancing angle deposition,[11] sol–gel processes,[12] and chemical vapor deposition[13] have recently been applied for NO nanostructure fabrication. Since the pioneering work by Sieber and co-workers,[14] nanoporous NO films grown via electrochemical oxidation (anodizing) of niobium have been the subject of investigation and already received some useful applications.[14,15] However, the major difficulty with this technology has been the aggressiveness of the electrolytes, limiting the film growth to about 500 nm, and irregular film morphology, resulting in the formation of microcone structures.[14] Even with the most recent advances in this approach, allowing a higher degree of morphology control and relatively stable growth of a thicker anodic film, the only possible structures are nanochannels or

pores that form in the film volume. [16,17]

Another electrochemical approach was pionired by Surganov and Mozalev,[18] in which one-dimensional (1-D) spatially-ordered metal-oxide nanostructures are synthesized via anodizing a thin layer of Al superimposed on a layer of different valve metal. In this approach, a nanoporous alumina is first formed from the Al layer, this being followed by processing the underlying metal through the alumina nanopores. Up to now, periodic arrays of 1-D hillock-like oxide nano- and microstructures have been synthesized from the Al/Ta,[19] Al/Ti,[20] Al/W,[21] and Al/Nb.[22] However, among the above metals, tantalum[23] and to a much smaller extent tungsten[21,24] have been known as the only valve metals capable of sustaining a high-potential reanodizing, i.e., post-anodizing polarization to a substantially more anodic potential, with the formation of pore-directed metal-oxide nanocolumns or rods. Should it be possible to grow such nanocolumns via anodizing niobium, more opportunities may arise for engineering the morphology, structure, and composition and for tuning functionality of NO films to address the needs of particular applications. The difficulty with niobium is that, despite the similarity in chemical properties of Ta and Nb, the electrochemical properties of these two metals differs significantly, resulting, for example, in the substantial difference in ionic resistivities, ion transport numbers, volumine expansion coefficient, and field crystallization behavior, thus challinging the efforts to achieve a sustainable oxide growth on niobium through alumina naopores.[25]

Here we demonstrate for the first time that an Al/Nb two-layer system can be electrochemically processed in such a way that it allows the growth of a self-organized array of anodic oxide on the niobium layer not only at the bottoms of pores but also much further along the pores, resulting in long-aspect-ratio NO nanocolumns, spatially-separated and upright-standing on a substrate. High-temperature annealing of the films helps achieve well-controlled crystallization and phase transition effects. The morphology-structure-property relationship for the synthesized NO nanostructures is determined by means of field-emission scanning (SEM) and transmission electron microscopy (TEM), X-ray photoelectron spectroscopy (XPS), time of flight secondary ion mass spectrometry (ToF-SIMS), X-ray diffraction (XRD), and energy dispersive X-ray (EDX) point analysis. A model of nucleation and growth of the NO nanocolumn arrays is proposed and experimentally justified. The electrical/dielectric properties of the films are assessed using electrochemical impedance spectroscopy (EIS) and through monitoring the behavior of electrical conductivity of the film material due to chemisorption of gas molecules on the film surface.

Experimental Section

Sample preparation

Double-side polished *n*-type Si wafers, 4" in diameter, 300-μm thick, with (100) crystal orientation and 4–40 Ω·cm conductivity, covered with a 200-nm layer of thermally grown SiO_2 were used as starting substrates. Niobium layers, of thicknesses ranging 110 to 250 nm, followed by aluminum layers, of thicknesses from 700 to 1000 nm, were successively sputter-deposited onto the wafers by a radio-frequency magnetron method. The use of silicon wafers was essential for providing a microscopically flat dielectric substrate to support the metal layers, for easy preparation of film fractures for SEM observations, and for avoiding ambiguity in interpreting results of XPS, XRD, and ToF-SIMS analyses. An oxide-coated electropolished aluminum foil, prepared as described elsewhere,[19] was also employed as the substrate for preparing ultramicrotomed sections for TEM and EDX. The wafers were cut into pieces of ca. 2 × 3 cm, which were then individually anodized in a specially designed two-electrode cell.[21] A Keithley 2410 programmed power supply was used as the anodizing unit. The anodizing electrolytes were aqueous solutions of 0.2 mol dm^{-3} oxalic ($H_2C_2O_4$) and 0.2 mol dm^{-3} sulphuric (H_2SO_4) acids due to the reasons explained elsewhere.[19,23] A number of acidic and neutral aqueous solutions were tested for reanodizing of the Al/Nb bilayer samples, with best results achieved to date in 0.1 mol dm^{-3} phosphoric (H_3PO_4) acid electrolyte. During each anodizing process, the temperature was maintained as constant as possible, typically within +1°C of the set value.

Film characterization

The Si-supported specimens were observed in a TESCAN MIRA field emission scanning electron microscope equipped with InBeam detector for secondary electrons and in an FEI Quanta 600 FEG environmental SEM. Cross sections of samples were examined by SEM in an FEI Strata DB235 dual beam SEM/FIB system combining an SEM with thermal emission tip for high resolution imaging and a FIB with gallium metal-ion beam source for nanoscale cutting. In the instrument, both beams are confocal and form an angle of 52°, and it is possible to simultaneously monitoring the progress using SEM and gas injection system for metal deposition. Prior to the sectioning, a layer of platinum, about 300 nm thick, was deposited over the sample surface for preventing top-surface damage. The FIB-made sections of the Si-supported samples and ultramicrotomed sections of the aluminium-foil-supported samples were examined in a JEOL JEM-2000FX transmission electron microscope with EDX facilities (the preparation details are available in ESI). An electron probe, of diameter about 5 nm, was employed to optimize spatial resolution and X-ray count rates.

XPS analysis was performed in a VG-ESCALAB 220iXL instrument equipped with an Al Kα monochromatised X-ray beam. The X-ray emission energy was 25 W with a 15 kV accelerating voltage focused to a spot of 500 × 500 μm. Typical operating pressures were better than 10^{-9} Torr. The emitted electrons were detected by a hemispherical analyzer at fixed pass energies of 50 eV for the survey spectra and 20 eV for the high-resolution spectra. The take-off angle was 90°. For the depth-profiling analysis, selected specimens were sputtered using an argon ion beam of 3 kV provided by a standard ion gun with a filament emission current of 2.5 μA and a spot size of 2 × 2 mm. The angle of incidence of the sputtering beam was 45° with respect to the substrate surface. After each sputter cycle (150 s), the XPS data were collected. Spectra were analyzed using CasaXPS software (version 2.3.16 PR 1.6). Gaussian (Y%)–Lorentzian (X%), defined in CasaXPS as GL(X), profiles were used for each component. A Shirley function was applied for background correction. All binding energies were referenced to the C 1s at 285.0 eV generated by photoelectrons emitted from

This journal is © The Royal Society of Chemistry [year]

carbon atoms in C-H bonds. ToF-SIMS analysis was carried out in an ION-TOF IV instrument (ION-TOF GmbH, Münster, Germany) with the depth profiles measured using the instrument in dual beam mode. A 10-keV Ar^+ ion beam of a current of 1.0 pA, rastered over a scan area of 5 × 5 μm, was used as the analysis probe. Surface sputtering was performed using a 3-keV Ar^+ ion beam at a current of 10 nA, rastered over an area of 200 × 200 μm. Both ion beams were directed under an angle of 45° with respect to the surface normal and were aligned in such a way that the analyzed ions were taken from the middle of the sputtered crater. The detection was made in the positive and negative ion modes. For each spectrum the mass scale was calibrated by using well-identified ions for the positive and negative spectra.

Diffraction patterns were taken from a Bruker-AXS D8-Discover diffractometer, equipped with parallel incident beam (Göbel mirror), vertical θ-θ goniometer, XYZ motorized stage, and a General Area Diffraction System (GADDS). The samples were analyzed in the reflection mode, and the area of interest was selected with the aid of a video-laser-focusing system. An X-ray collimator of 500 μm system allowed the analysis of a mean area represented by an ellipsoid with a constant short axis of 500 μm and a variable long axis of 1500 up to 600 μm. The X-ray diffractometer was operated at 40 kV and 40 mA to generate CuKα radiation. The GADDS detector was an HI-STAR (multiwire proportional counter of 30 × 30 cm with a 1024 × 1024 pixel) placed at a 15-cm distance from the sample. Three frames were collected in the reflecting mode covering 16-85° 2θ. The exposition time was 300 s per frame, and it was γ-integrated to generate the conventional 2θ vs. intensity diffractogram. The experimental diffractograms were fitted with the crystal structure (Rietveld analysis) for the phases identified with the aid of TOPAS software (V4.2, 2009, Bruker AXS GmbH, Karlsruhe, Germany). With the same software, the cell parameters and the mean crystallite size of detected phases were determined using the Double Voigt approach. The wt% of the phases involved was estimated by refining the Rietveld scale factor. The instrumental contribution was obtained from a sample of LaB_6 (SRM 660a) analyzed under the same conditions and was considered prior to estimation of the crystallite size.

Estimation of functional properties

EIS measurements were carried out in 0.5 mol dm^{-3} H_3BO_3/0.05 mol dm^{-3} $Na_2B_4O_7$ solution (pH 7.4) at 296 K. A μAutolab III/FRA2 Metrohm Autolab Potentiostats/Galvanostats was used as the impedance analyzer linked to PC via a USB cable. The signal amplitude was 140 mV over the frequency range of 10 mHz – 800 kHz. The measured impedance data were analyzed by a computer simulation and fitting program written in Autolab Nova Software. Gas-sensing tests were performed with a fully automated setup, where the desired concentrations of gases were obtained from calibrated gas cylinders by means of mass-flow controllers. Dry air was used as balance gas. The total gas flow was adjusted to 100 ml min^{-1}. The electrical resistance in the presence of dry synthetic air or the diluted gas/vapor was monitored using a Keithley 2410 Source Meter controlled by LabVIEW software via PC. Data acquisition was performed at a sampling rate of 0.5 sample s^{-1} by a program written in LabView. The operating temperature of the sensors, in the range of 100-350°C, was set in 50-degree steps by applying calibrated constant voltages to micro-heaters prepared on ceramic substrates.

Results and discussion

The formation-morphology relationship

From the anodizing/reanodizing behavior revealed for the Al/Nb bilayer (Figure 1), it is anticipated that the main processes to achieve the field-assisted growth of self-organized nanostructured NO involve the following three stages. First, a porous anodic film grows on the Al layer. Then, NO develops within the alumina barrier layer. Finally, NO nanocolumns or rods grow along the alumina pores and, possibly, in-depth of the niobium underlayer. As an example, Figure 1a shows the potential-time and current-density-time responses recorded during the galvanostatic-potentiostatic anodizing in 0.2 mol dm^{-3} $H_2C_2O_4$ electrolyte of an Al/Nb bilayer on an oxidized Si wafer. During the galvanostatic polarization, a porous alumina grows with a constant rate, at a steady-state potential of 52 V, reaching the underlying niobium metal at the end. At the given current density and film thickness, in ~3 min the alumina barrier layer touches the niobium metal, and the potential begins to rise, and then the power supply is switched into the constant-potential regime, preventing the oxide from further growth, this being accompanied by a current decay over about 2 min.

The potential-time and current-time responses for reanodizing to 310 V of the same specimen are shown in Figure 1b. An initial potential surge of about 60 V is evident due to the presence of anodic NO under the pores. As at the initially set current value the potential rose at a gradually decreasing rate, indicating the insufficient driving force for a stable oxide growth, the current was raised (adjusted) twice (points 1 and 2 in Figure 1) to keep a uniform potential growth rate, which is associated with the linear segment in the potential-time curve between 65 and 310 V. Thus, the rise in the formation potential during the constant-current reanodizing confirms the field-assisted growth of anodic oxide on niobium while the final current decay, without overshoots and substantial fluctuations, is a good sign of completing the ionic transport through the anodic film at the established field strength.[26] It should be noted that, during the higher-potential reanodizing experiments, the potential was closely approaching the value of 550 V, this being however accompanied by increasingly occurring potential fluctuations (current overshoots), which were likely due to the combined effect of stress generation during the film growth and the beginning of NO field crystallization, resulting in destructive oxygen evolution.[25,27] The smooth growth of a defect-free anodic film on niobium metal in the range of formation potentials up to 450 V was achieved for the first time due to great flexibility offered by the porous-alumina-assisted anodizing approach and the appropriate combination of technological, electrical, and electrolytic formation conditions. Digital optical photos and SEM images confirming the defect-free formation of large-surface-area NO nanostructures are available in ESI)

Figure 2 shows SEM images of the surface and sectional views of the two types of anodic films derived from the same initial Al/Nb bilayer onto an SiO_2/Si substrate: (1) anodized at 52 V in the oxalic acid electrolyte (Figure 2a-c) followed by reanodizing in the phosphoric acid electrolyte to potentials up to 450 V (Figure

2d-i) including that resulted from the dissolution of the alumina overlayer in a selective etchant prepared as described elsewhere[28] (Figure 2f-i); (2) anodized at 26 V in the sulphuric acid electrolyte followed by reanodizing to 150 V and dissolution of the alumina layer in the selective etchant (Figure 2g-l).

Arrays of nanosized protrusions, presumably of NO, mostly having root-like substructure at their bottoms, derived from the Nb underlayer, are revealed in the micrographs of Figure 2b-c. Comparing the geometry and sizes of the observed nanostructures with the alumina pores, one may see that the roots grow in the alumina barrier layer right under the pores while the tops are obviously wider than the alumina pores and already penetrate the pore bottoms, slightly coming out over the alumina barrier layer. The roots are surrounded by a network of unoxidized aluminum metal, which still remains after the treatment in the selective etchant (Figure 2c).

In the images of the reanodized specimens, relatively uniform grey bands are evident within the film sections between the remaining niobium metal and the alumina layer (Figure 2i-g and e). Columns of material, generally similar in contrast to the bands, up to about 800 nm long, extend at regular intervals from the band outward into the pores in the alumina film. With reference to the previous works,[21,23] the band and columns represent NO-containing regions formed over the residual niobium layer, which is pointed out in Figure 2f, g, i, and k. Thus, two layers are distinguished in the anodized/reanodized samples: an upper, structured layer comprising the nanocolumns penetrating the pores and a lower, continuous layer of relatively uniform thickness lying between the upper layer and the residual niobium or the SiO_2 substrate if the metal is fully consumed. For the oxalic-acid formation electrolyte, the mean column diameter is 55 nm, which is ~1.8 times the average pore size in the alumina film (30 nm). Similar tendency was revealed for the sulphuric-acid-made sample (26 V formation potential), in which the average column diameter is 22 nm while the average pore size is only 12 nm. The main stages of film growth, with the relationship between the film layers, are depicted in Figure 3.

Film composition

The specimen analyzed by ToF-SIMS was the "alumina-free sample" (as shown in Figure 2i and 3f). ToF-SIMS was employed to analyze chemical composition of the films as the method allows to image the distribution of molecular ions and their associated fragments that are emitted from monolayer film surface. Figure 4a shows the ToF-SIMS depth profiles of the following characteristic negative and positive ions from the alumina-free specimen: PO_3^- (m/z=790), OH^- (170), Al^+ (270), Si^+ (280) NbO^+ (1089), and Nb_3^+ (2787). The Si^+ and Nb_3^+ fragments are used as marker elements to distinguish the region beneath the anodic film while the other species originate from the film material and their relative depth profiles may help understand the distribution of elements and chemical compounds throughout the film. The diagram under the ToF-SIMS profiles relates approximately the regions in the analyzed sample with the emitted ions.

Examination of chemical composition and bonding states in the anodic films was further continued by XPS. The specimens analyzed were (1) the "pore-free" sample (as in Figure 2e and Figure 3e), (2) the alumina-free sample, and (3) the vacuum-annealed alumina-free sample (heated over 2 hours at 10^{-5} Pa and then cooled down to room temperature). The presence of C, Nb, O, Al, P, and Si was identified in the wide-scan survey spectra recorded on the surfaces of all the samples. Narrow-scan C 1s, Nb 3d, O 1s, Al 2p, P 1s, and Si 2p spectra were recorded to analyze the core levels of the detected elements. Representative XPS atomic concentration profiles for the alumina-free sample are displayed in Figure 4b. Unlike the ToF-SIMS profile, the XPS concentration profiles were recorded during the sputtering of the columnar film part only. For all the XPS data collected from samples not sputter-cleaned prior to the analysis, the peak-fitting of C 1s spectra was guided by the strategy explained in the Electronic Supplementary Information (ESI) with reference to C 1s spectrum of the alumina-free sample;[29] the main peak-fitting parameters for the XPS spectra are also given there.

Figure 5a shows an Nb 3d spectrum of the alumina-free sample surface. The curve-fit peaks in the lower energy edge of the spectrum are zoomed-in in Figure 5b. Two doublets of appropriately constrained peaks (Nb $3d_{5/2}$ and Nb $3d_{3/2}$) are used to reproduce the spectrum. The Nb $3d_{3/2}$ peak for each species is constrained to be at a fixed energy increment of 2.75 eV above the Nb $3d_{5/2}$ peak, and the intensity ratio of the Nb $3d_{5/2}$ and Nb $3d_{3/2}$ peaks is fixed to 3:2. The full widths at half maximum (FWHM's) for Nb^{5+} $3d_{5/2}$ and $3d_{3/2}$ peaks are constrained to be equal to each other while FWHM's for the peaks in the Nb^{n+} 3d doublets (where n<5+), which are likely structurally loosely ordered, are slightly broader. The highest-intensity doublet with binding energies (BE's) of 207.3 eV (Nb $3d_{5/2}$) and 210.05 eV (Nb $3d_{3/2}$) is associated with photoelectrons emitted from Nb atoms with +5 oxidation state (Nb^{5+}), i.e., stoichiometric Nb_2O_5[30,31] The lower-intensity well-defined doublet with BE's at 205.65 eV (Nb $3d_{5/2}$) and 208.4 eV (Nb $3d_{3/2}$), shifted to –1.65 eV from the dominating spectrum component, is associated with Nb $3d_{5/2}$ and $3d_{3/2}$ electrons emitted from niobium atoms with +4 oxidation state (NbO_2).[32] No peaks attributed to metallic niobium are present in the spectrum.

Figure 5c shows the Nb 3d spectrum of the vacuum-annealed specimen. The highest-intensity doublet with BE's of 207.35 eV (Nb $3d_{5/2}$) and 210.1 eV (Nb $3d_{3/2}$) dominates in the spectrum and is associated with photoelectrons emitted from niobium atoms in stoichiometric Nb_2O_5. Besides, the spectrum reveals two more chemical shifts from the Nb^{5+} level, which correspond to niobium suboxides (see also the enlarged view in Figure 5d). The lowest-energy doublet with a Nb $3d_{5/2}$ BE at 203.85 eV, shifted to +1.65 eV from the bulk level (202.2 eV for Nb^o $3d_{5/2}$),[33] is generated by photoelectrons emitted from Nb atoms with +2 oxidation state (Nb^{2+}) in NbO. The second low-intensity doublet with a Nb $3d_{5/2}$ BE at 205.5 eV, shifted to +3.3 eV from the bulk level, is due to Nb^{4+} ions in NbO_2.[32]

The Nb 3d spectrum of the pore-free sample, in which the photoelectrons are collected from column tops only, is shown in Figure 5e. It is easily fitted by a perfect high-intensity doublet with BE's of 207.2 eV (Nb $3d_{5/2}$) and 209.95 eV (Nb $3d_{3/2}$) and equal FWHM's of 1.07 eV, which is associated with structurally well-ordered stoichiometric Nb_2O_5.

The analysis of the curve-fitted Nb 3d spectra reveals clearly that niobium suboxides are found already in the as reanodized (unannealed) alumina-free sample surface and are most likely

This journal is © The Royal Society of Chemistry [year]

located in the lower film layer, not in the column material, which is mostly niobium pentoxide. Annealing the sample in vacuum promotes the formation of more suboxides in the film composition while keeping the pentoxide dominating, at least on the sample surface.

The Al 2p spectrum of the alumina-free sample is shown in Figure 5f. The spectrum is well reproduced by a symmetrical singlet with a BE energy of 74.5 eV and a FWHM of 1.4 eV, which is associated with alumina (Al_2O_3).30**Error! Bookmark not defined.** When the specimen is Ar^+ ion sputtered, the peak intensity monotonically decreases, the peak being visible until the last, 20th sputter cycle (Figure 4b). The presence and distribution of alumina in the film is also obvious from the image of Al^+ characteristic fragment of the ToF-SIMS profiles (Figure 4a). Alumina was also detected in comparable concentration in the vacuum annealed columns. The SEM images in Figure 4 show the surface of the alumina-free sample before (top) and after (bottom) the Ar-ion sputtering. The tips the etched columns are likely the former column bases that still remain while the deeper rods are derived from the film layers that were formally beneath the columnar part of the film. This sort of morphology develops because of the simultaneous etching of the material composing the columns and surrounding columns. This phenomenon leads to longer profiles with uncertain interfaces. Nevertheless, the columns were shortened, thinned, and round-etched quite smoothly, and no preferential erosion of the column material is observed from the direction of Ar-ion beam. Thus, the XPS, ToF-SIMS, and SEM results reveal that alumina is present and evenly dispersed in the outer layer of the column material.

Figure 5g and h shows the O 1s spectra of the initial and Ar-ion sputtered surfaces of the alumina-free sample. The curve-fitting of the O 1s line is very complex. Besides the usual O 1s peak components present in the outmost film layer due to H_2O (chemisorbed water) at a BE of 533.5 eV and OH (hydroxylated region) at a BE of 532.4 eV, there are two more well-resolved peaks of relatively higher intensities in the lower-energy range. The most intensive peak at 530.5 eV is due to the oxygen species O^{2-} in niobium oxide while the smaller peak at 531.6 eV is assigned to O^{2-} species bonded with Al^{3+} in the alumina-containing region. With the Ar ion sputtering, the relative intensity of the 531.6-eV peak (O^{2-} in Al_2O_3) decreases, due to the diminution of alumina portion. Further, instead of the two higher-energy peaks associated with OH and H_2O, a singlet peak at 532.8 eV is found in the O 1s spectrum of the Ar ion sputtered alumina-free surface. It is commonly accepted that the peak positions of the hydroxyl oxygen (OH) and the oxide species (O^{2-}) are usually 1.1-1.5 eV apart with an approximately equal FWHM while bonding of water molecules causes energy shifts of about +3 eV from the O^{2-} peak position in O 1s spectrum.[34] Expecting no chemisorbed water in the film depth and comparing the shift of the 532.8-eV peak towards the Nb_2O_5-associated peaks (+2.35 eV) and the Al_2O_3-associated peak (+1.0 eV), we assign this higher-energy peak to the hydroxilated part of the alumina-containing region. The behavior of OH^- ion fragment in the ToF-SIMS depth profile (Figure 4a) additionally justifies this conclusion.

The presence of minor atomic concentrations of P and Si was detected via tracking the P 2p and Si 2p lines for the alumina-free sample (Figure 4b). Soon after the beginning of sputtering, the P 2p spectrum consisted of two symmetrical peaks with BE's of 133.8 eV (P^{5+} ions bound in phosphate)[35] and 129.3 eV (P^o in metallic phosphorus),[30,31] as shown in Figure 5i. The intensity of the lower-energy peak increased with sputtering time while the higher-energy peak gradually diminished. The long-lasting image of phosphate fragment PO_3^- in the ToF-SIMS depth profile (Figure 4a) implies that the evolution of the P 2p spectrum is due to a sputtering-induced effect.[29,34] Thus, one may conclude that P-containing species are incorporated in the column depth, though to a smaller extent then alumina.

The presence and depth profile of Si-containing species was revealed via tracking the Si 2p spectrum within the film depth. The surface-registered Si 2p spectrum is fitted by a symmetrical single peak with a BE of 102.3 eV (Figure 5j). This peak is not associated with SiO_2, in which the BE for Si 2p electrons is 103.2 eV.[30] Likely, the silicon is present in the structure of a silicate compound, in which Si^{4+} anions are coordinated with Nb^{5+} or Al^{3+} cations. The silicate may form due to Si^{4+} ions originating from the SiO_2/Si substrate and migrating outward through the pathways in the remaining niobium metal, then in the lower film layer, and finally along the columns, contributing to the growth of the anodic film at the electrolyte/NO interface.

Table 1. Results of EDX point analysis of ultramicrotomed sections of the as reanodized sample (SEM image in Figure 6f): atomic concentrations in the Al-Nb-O system, and empirical formulas of the niobium oxides determined in the areas (spots) marked on Figure 6f.

spot	Nb (at%)	Al (at%)	O (at%)	Formula
1	79	1.33	19.67	$Nb_{1}O_{0.22}/Al_2O_3$
2	31.52	1.65	66.83	$Nb_{1}O_{2.04}/Al_2O_3$
3	22.27	8.08	69.65	$Nb_{1}O_{2.58}/Al_2O_3$
4	14.81	12.38	72.82	$Nb_{1}O_{3.66}/Al_2O_3$
5	16.41	14.18	69.13	$Nb_{1}O_{2.91}/Al_2O_3$
6	11.38	18.46	70.17	$Nb_{1}O_{3.73}/Al_2O_3$

The graded oxide stoichiometry

Figure 6a-b shows TEM images of the individual columns that were scratched away from the alumina-free sample, collected on a cupper grid, observed in a TEM, and analyzed by EDX point technique. The presence of Nb, O, Al, and relatively smaller amount of Si is well identified in the corresponding X-ray spectrum in Figure 6c. A TEM image of the FIB-made lamella of the as reanodized sample (the porous alumina was not dissolved) is shown in Figure 6e. On the image, the 3 conditionally marked spots are the positions of the electron probe used in the EDX analysis (the X-ray spectra are available in ESI). Summarizing the results, the high-intensity Nb and O peaks and low-intensity Al and Si peaks are registered within the column (spot 2). No peaks of Al are found in the residual niobium metal (spot 3), and

no peaks of Nb are registered in the top part of the porous alumina film where the columns are not expected to grow (spot 1). The Cu peak is from a copper grid used for holding the sections in the TEM chamber while the signal of Pt comes out from the platinum overlayer, which partly penetrates the pores. This eventually confirms the presence of Al and Si in the column material and shows the degree of filing the pores by the niobium oxide. The high-resolution TEM images of fragments of the lamella are shown in Figure 6d, g, and h. On these images, the round spots are the areas impacted by the Ga ions used for sputtering the sample surface in the FIB technique employed here. Three regions (*a*, *b*, and *c*) with dissimilar physical properties are well distinguished within the column section, the interpretation is given later in the text.

Further, an attempt was made to perform a quantitative assessment of the amounts of NO and alumina in the different parts of the as reanodized film. Three ultramicrotomed sections, each about 20 nm thick, were prepared for this purpose (Figure 6f). The 5-nm electron probe was pointed to 6 positions along the depth of each section. The average atomic concentrations of elements in the Al-Nb-O system calculated from the three sets of measurements are given in Table 1. The empirical formulas, giving the average atomic proportional ratio in the Nb-O system calculated from the data obtained from all the sections are also shown in the table (the complete set of EDX data for each section is available in ESI). The empirical formula of the NO in the lower film layer (spot 2) indicates the formation of niobium suboxide that is referred to as NbO_x, where Nb^{4+} is assigned as the upper limit (NbO_2) for the oxidation state of NbO_x. The empirical formula in the bottom part of the columns (spot 3) corresponds well to Nb_2O_5 molecular formula. The abundance of oxygen detected within the columns (spots 4, 5, and 6) may arise from an electron-beam-assisted generation of bare cation vacancies and intersitial type of point defects in the alumina and especially in the nanosized areas of niobium oxide via the following mechanism of producing electronic defects that involve changes in valence states:

$$Nb^{n+} + e^- \rightarrow Nb^{(n-1)+} \quad (1)$$

The remaining niobium metal (spot 1) comprises about 20at.% of oxygen, which originates from the air-formed oxide film that grows on both sides of the metal slice and may eventually consume up to 15% of the slice thickness. Additionally, some oxygen may have already been present in the initial magnetron-sputtered Nb film.

Based on the XPS and EDX analysis results we conclude that the columns are composed of amorphous Nb_2O_5 (major amount), Al_2O_3, Si-, and P-containing species (minor amounts) while the lower film layer is likely NbO_2. Apart from the crystallization effect to be considered in the following section, the annealing of the alumina-free film in vacuum at 550^{o}C increases the relative concentration of NbO_2 and promotes the formation of NbO suboxide, with a surface concentration of ~6%.

Crystallization and phase transition effects

The specimens analyzed by XRD were (1) the unannealed alumina-free sample (as in Figure 3f), (2) the air-annealed alumina-free sample, and (3) the vacuum-annealed alumina-free sample. The 2-D diffractograms from which the conventional diffractograms were obtained are available in ESI. The spots associated with the Si wafer appear different because they are very sensitive to the wafer orientation inside the diffractometer. Figure 7 shows the experimental, calculated, and difference diffractograms of the air-annealed and vacuum-annealed samples. For both samples, in the analyzed range there is no evidence of peaks associated with any crystalline phases of Al_2O_3 (at the available detection limit). For the air-annealed sample (Figure 7a), in the range of 20-85° 2θ angles, all the detected diffraction peaks are from the orthorhombic Nb_2O_5 phase (space group (sg) Pbam), except for the peak associated with the Si wafer. For the vacuum-annealed sample (Figure 7b), the crystalline phases identified are metallic Nb (sg $Im\bar{3}m$), NbO (sg $Fm\bar{3}m$), β-NbO_2 (sg $I4_1$), and Nb_2O_5 (sg Pbam). The crystal structures for each phase were found in the ICSD database and are presented in the ESI, being accompanied by the results of quantitative analysis of the experimental diffraction patterns.

The main revelation from the XRD analysis is that the initially amorphous NO crystallizes to the Nb_2O_5 phase due to the annealing in air and to the NbO-NbO_2-Nb_2O_5 sequence of phases due to the annealing in vacuum. In the vacuum-annealed sample, the calculated wt% of the phases (shown in ESI), reflects the process of diffusion of oxygen from the niobium pentoxide and the formation of crystalline phases of the lower niobium oxides β-NbO_2 (6.98 wt%) and NbO (15.61 wt%), this being followed by dissolution of the released oxygen ions in the niobium substrate.[33] From comparison of the XPS, EDX, and XRD results, we conclude that the portion of crystalline niobium pentoxide is mostly located in the uppermost column layer while the concentration of crystalline niobium suboxides increases towards the niobium-oxide/niobium interface.

The model of film growth

Combining the previous experience in anodizing the Al/Ta couple[23] with the experimental findings of the present work, we were able to develop a model for the growth of nanostructured oxide on niobium during its porous-alumina-assisted anodizing followed by high-potential reanodizing. The main phases of film growth are depicted in Figure 8 and supported by selected SEM views showing the development of anodic oxide nanostructures at the respective interfaces. According to the model, over the first current decay (Figure 8b), NO grows due to the local oxidation of the Nb underlayer under the alumina cells. During this process, alumina is expected to continuously dissolve at the barrier-layer/NO interface due to dissociation of the Al-O bonds under the high field. The O^{2-} ions released from the dissociating barrier layer may participate in further oxidation of niobium while the released Al^{3+} ions may migrate outwards and are most likely expelled in the electrolyte. Because of the pore-directed, regular current distribution, cross-migration of Nb^{5+} and O^{2-} ions takes place along few narrow and perpendicular to the substrate sub-channels in the barrier layer right under the pores (Figure 8b). The formation of such nanochannels for ion migration results in the root-like structure of the lower parts of NO protrusions that grow during the first current decay and are well seen in Figure 2b and c. The local consumption of niobium proceeds at a faster rate than the oxidation of the adjacent aluminum since anodic niobium oxide has lower ionic resistivity than anodic alumina.[19] That is why the oxidation of the adjacent aluminum is practically ceased over the whole span of current decay, so that an aluminum

This journal is © The Royal Society of Chemistry [year]

network remains around the NO protrusions even after completing the anodizing, and it is well observed in Figure 2c. This finding does not generally contradict to a previous work by Habazaki and co-workers,[36] reporting that, during the anodizing of Al superimposed on Nb in barrier-type electrolytes, randomly occurring NO nano-needles penetrate and irregularly mix with the upper alumina. However, the findings of our work reveal clearly that the ionic transport and anodic oxide growth become increasingly systematic when the Nb metal is reanodized through the alumina nanopores, which determine the local spots for nucleation and growth of the NO nanocolumns. The enlarged and fully solid (root-free) tops of the NO protrusions (see also Figure 2c) result from merging the sub-nanochannels into a relatively wider pathway (Figure 8c), which is believed to happen because of the beginning of oxide growth inside the pores and the ion migration within the outer part of the alumina cell walls. This may be due to the differences in the properties of this outer part of the cell walls (layer *3*), the intermediate layer *2*, and the stoichiometric Al_2O_3 in the deepest region of the alumina barrier layer and cell walls (layer *1*), as shown in Figure 8a and revealed in the previous work on anodizing Al/Ta layers[23] A higher ionic conduction of layer *3* can be expected due to the structural imperfections, cation vacancies, electrolyte species, bound water, protons, and other defects that may be present in the layer.[37,38] When the migrating niobium cations reach layer *3*, niobium oxide continues to grow along the enlarged channel decided by the configuration of this "contaminated" part of the cell.[19]

During the reanodizing, the Nb layer is further consumed and new, columnlike oxide continuously forms and is directed into the pores via cross-migration of niobium and oxygen ions, with the formation of more nanoroots (migration channels) or with expanding the existing migration pathways in the alumina barrier layer (Figure 8d). Importantly, the aluminium network that still remains after the anodizing is then gradually oxidized during the reanodizing, being completely consumed at about 80 V, which is confirmed by the XPS analysis. The fact that the columns are wider than the pores (Figure 8e) is likely due to replacement phenomenon that occurred during the column growth inside the alumina nanopores, like in the case of Al/Ta anodizing.[39] The oxide growth along the pores competes with widening the column bases, which tend to group to create regions of increased dimensions until neighbouring bases merge and continue to grow as a uniform, solid layer of niobium oxide under the columns (well observed in Figure 2i, f, and i), since the progress of oxidation also consumes aluminum that remains around the alumina cells and thus niobium is continuously involved in the formation of new oxide, as shown in Figure 8d and e. The relationship between these competing phenomena, influencing the development of the upper and lower film layers, is probably determined by the volume expansion factor, the transport numbers for niobium species, which might be a complex value,[21] and the ratio of ionic resistances of the NO and the alumina encircling the columns.

Clearly, the situation with the Nb underlayer contrasts substantially with that for the W or Ta underlayers,[21,23] because the difference between the ionic resistivities of the NO and the contaminated part of the alumina cell wall is more obvious. What might be closely related to the present case is the Al/Ti couple[20] since the resistivity of anodic titania is quite comparable to that of anodic niobia. Comprehensive experimental study on anodizing behavior of Al/Ti metal layers will be performed in due course.

Electrical/dielectric properties

As the first step to reveal the functional properties of the NO nanostructures developed here and to possibly tune them to meet the requirements for particular applications, such as electrical capacitors and gas sensors, we have undertaken a study on electrical/dielectric behavior and chemiresistive gas sensitivity of the selected amorphous and crystalline anodic NO films synthesized to date. Figure 9 shows the impedance bode diagrams for the Al/Nb specimen anodized/reanodized at 51 V/200 V in the oxalic/phosphoric acid electrolytes before and after selective dissolution of the alumina overlayer. The diagrams suggest a simple equivalent circuit (Figure 9b), where C is the parallel capacitance of the film, R_f is the parallel resistance of the film, and R_{sol} is the resistance of the solution. From the EIS data, the dielectric behavior of the as reanodized anodic films, where the effective dielectric thickness is a combination of the lower film layer and the composite niobium-aluminum mixed oxide layer (Figure 9c), is very close to the behavior of an ideal capacitor. However, the dielectric properties of the same film obviously deteriorate after the alumina is dissolved, as in Figure 9d. This implies that the film properties change from the perfect dielectric to semiconducting, without yet any heat treatment applied to the sample. This is explained by the compositional profile of the film: the lower film layer, comprising NbO_2, which is *n*-type semiconductor, becomes exposed to the solution while the columnar part of the film, which is mainly dielectric Nb_2O_5, becomes practically short-circuited by the solution and does not contribute to the measured impedance value.

The present findings suggest that the transformation from the dielectric to *n*-type semiconductor behavior of the reanodized Al/Nb bilayer may be tuned through altering the amount of the alumina in the film composition by partially dissolving the alumina component in the film. More challenges for tailoring the electrical/dielectric properties of these complex metal-oxide nanostructures are associated with post-anodizing chemical treatments and low- and high-temperature annealing in air and vacuum, so as to impact the chemical states of the NO and diversify crystallization and phase transition effects in the films.

Gas sensing properties

For gas-sensing experiments, the oxalic/phosphoric-acid-made, air-annealed alumina-free film (as in Figure 2f) was employed. Pairs of platinum interdigitated electrodes, with 50-μm spacing, placed over the NO column array and pairs of platinum micropads for contacting the electrodes were prepared by sputter-deposition and lift-off photolithography. The film was attached to a miniaturized hotplate allowing operating temperatures up to 350°C. A sketch of the test sensor complemented by the SEM images of the sensor and the film/electrode interface are presented in Figure 10a-d. Hydrogen (H_2) and ethanol (C_2H_6O) were employed as gas analytes. Gas sensing ability of the film was assessed via measuring the resistance between the electrodes in the presence of each gas.

The experimental resistance-temperature response recorded in air is shown in Figure 10e. The systematic decrease in sensor

resistance with raising the operating temperature is attributed to *n*-type semiconductor behavior of the nanostructured NO. As an example of the film chemisorption ability, Figure 10f shows the time-resolved resistance behavior in the presence of 1000 ppm of H_2 at operating temperatures of 250 and 300°C. From the figure, the sensor responds to hydrogen very fast, with rather stable baseline, and the response and recovery times shorter than 1 min at 300°C. This characterizes the sensor as one of the fastest in the niche of nanostructured metal-oxide gas sensing films.[40,41] Comparative characteristics of best hydrogen-sensing nanostructured active layers found in the are available in ESI). Further, the sensor resistance appeared to be well-dependent on the gas concentration, with the detection limit not worse than 100 ppm (no measurements were yet performed in the lower concentration range). The achievement is due to the periodic two-dimensional nanosized architecture of the NO film complemented by the nanocrystalline structure and the systematic chemical composition, with the 2-D (depth and width) atomic concentration and niobium ion oxidation state profiles, and a substantially enlarged active surface area of the film as well. These all contribute to increasing the rate of adsorption and diffusion processes, to enhancing the redox reactions between the oxide and gaseous species, and to making the whole film volume involved in interaction with the gas.

The sensor behavior towards ethanol was quite different. The sensor response/recovery time in the C_2H_6O was incomparably long (25/200 min). On the other hand, the detection limit for ethanol appeared to be as low as 2 ppm already at 150°C, as shown in Figure 10g. This characterizes the nanostructured NO-based sensor as highly sensitive and low-power consuming for ethanol detection.[42] Comparative characteristics of best ethanol-detecting sensors with relevant references are available in ESI). This finding may be a stepping stone for the development of chemiresistive semiconductor sensors selective towards different gases whose interaction with metal-oxide semiconductors is based on principally the same, electron donating (reducing) effect.

Gas sensing mechanism

Considering the presence of stoichiometric crystalline Nb_2O_5 in the composition of sensing layer and with reference to recently reported H_2-sensing mechanism for the WO_3 nanostructures,[43] we assume that, in a hydrogen atmosphere molecular hydrogen dissociates on the surface of the platinum electrodes, giving hydrogen ions and electrons:

$$H_2 \rightarrow 2H^+ + 2e^-, \quad (2)$$

which diffuse into the grain boundaries of the NO nanofilm and reduce Nb^{5+} centers in the Nb_2O_5 crystal lattice to lower oxidation states (the resistance decreases):

$$Nb_2O_5 + 2H^+ + 2e^- \rightarrow 2NbO_2 + H_2O \quad (3)$$

When the hydrogen gas is purged from the chamber by a dry air flow, the film stoichiometry is restored (the resistance returns to its initial value):

$$4NbO_2 + O_2 \rightarrow 2Nb_2O_5 \quad (4)$$

The sensing mechanism towards ethanol might also be based on the above reactions (2-4) since molecular hydrogen may be generated from ethanol decomposition on the platinum electrodes according to any of the following reactions[44]:

$$C_2H_5OH \rightarrow CO + CH_4 + H_2 \quad (5)$$

$$C_2H_5OH \rightarrow C_2H_4O + H_2 \quad (6)$$

The following reaction may also occur because hydrogen in air partly reacts with oxygen at the surface of the Pt microelectrodes and is oxidized to water:

$$C_2H_5OH \rightarrow H_2O + CO_2 + CH_4 + 2H_2 \quad (7)$$

However, since the sensor response to ethanol appeared to be incomparably slower than that to hydrogen, it is most likely that the ethanol-sensing mechanism is based on a more commonly believed theory that considers the electrical conductivity in a metal oxide as being due to non-stoichiometric composition as a result of oxygen deficiency. According to this mechanism, when the NO film surface is exposed to air, oxygen molecules are adsorbed at the surface resulting in the formation of O_2^-, O^-, O^{2-} ions, thus decreasing the number of charge carriers near the surface and giving rise to a depletion region. When the film is exposed to ethanol vapour (reducing gas), oxygen species react with ethanol as follows:

$$C_2H_5OH + 6O^- \rightarrow 3H_2O + 2CO_2 + 6e^- \quad (8)$$

Reaction (7) takes place only if the gas is completely oxidized on the sensor surface. Partially oxidized gas may not change the sensor resistance drastically or the surface reactions may retard, which might be the case of our NO nanofilm. This may happen because the amount of oxygen adsorbed on the film surface would depend on the number of Nb_2O_5 misfits to adsorb the oxygen which in turn would oxidize the gas.[45] If this is the case, to speed up the oxidation of ethanol a more nonstoichiometric film composition, which results from the annealing in vacuum, should be advantageous. Sensing behaviour of the oxygen-deficient NO nanofilm will be examined in a future work on gas-sensing properties of the NO nanofilms.

Conclusions

In our work to date, we have succeeded in the formation of niobium oxide nanofilms with the self-organized nanocolumn morphology via applying a blend of anodizing, reanodizing, and annealing techniques to sputter-deposited Al/Nb metal layers. Due to the smart formation approach, the film growth proceeds smoothly, without dielectric breakdown and destructive field crystallization and physical defects, which are usual attributes for anodic and thermal oxide growth on niobium, limiting the techniques available for well-controlled preparation of NO films. The amorphous NO films synthesized here possess nearly perfect dielectric properties, so that they may become an ideal substitute for Ta_2O_5 in wet- and solid-electrolyte tantalum capacitors. The vacuum-annealed films exhibit pronounced *n*-type semiconductor behavior and reveal advanced functionality as active layers for semiconductor gas microsensors with the excelent sensitivity to ethanol and the fastest response to hydrogen. Making the film formation processes compatible with standard micromachining technologies is among future opportunities and will be addressed in due course.The formation approach may be of further practical importance as it introduces technically simple, well reproducible, cost-effective, and environmentally friendly way that may also be suitable for growing metal-oxide nanostructures on some other transition metals and their alloys, with tunable functionality and for a variety of potential applications.

This journal is © The Royal Society of Chemistry [year]

Acknowledgements

Research leading to these results was supported in part by the Czech Science Foundation (GAČR) grant no. 14-29531S, by EU grant COST MP0901 'NanoTP', and by MINECO grant no. TEC2012-32420. E.L. is supported by the ICREA Academia Award.

Notes

[a] *Laboratory of Microsensors and Nanotechnology (LabSensNano), Central European Institute of Technology (CEITEC), Brno University of Technology, Technicka 10, 616 00 Brno, Czech Republic, E-mail: mozalev@feec.vutbr.cz*

[b] *MINOS-EMaS, Universitat Rovira i Virgili, Avda. Països Catalans 26, 43007 Tarragona, Spain*

[c] *Chimie des Interactions Plasma-Surface (ChIPS), CIRMAP, Research Institute for Materials Science and Engineering, University of Mons, 20 Place du Parc, B-7000 Mons, Belgium*

[d] *Materia Nova Research Center, 1 Avenue Nicolas Copernic, B7000 Mons, Belgium*

[e] *Scientific Service, Universitat Rovira i Virgili, Avda. Països Catalans 26, 43007 Tarragona, Spain*

[f] *Division of Materials Chemistry, Faculty of Engineering, Hokkaido University, Kita-ku, N-13, W-8, Sapporo 060-8628, Japan*

† Electronic Supplementary Information (ESI) available: Details of the XPS analysis, EDX point analysis of the FIB-made lamella and the ultramicrotomed film sections, 2-D diffractograms and interpretation of the XRD results, comparative analysis of the gas sensing characteristics, sample preparation details. See DOI: 10.1039/b000000x/

References

1. S. Singh, H. Kaur, V. N. Singh, K. Jain and T. D. Senguttuvan, *Sens. Actuators B*, 2012, **171- 172**, 899- 906.
2. M. E. Gimon-Kinsel and K.J. Jr. Balkus, *Microporous and Mesoporous Mater.*, 1990, **28**, 113- 123.
3. R. A. Rani, A. S. Zoolfakar, J. Z. Ou, R. A. Kadir, H. Nili, K. Latham, S. Sriram, M. Bhaskaran, S. Zhuiykov, R. B. Kaner and K. Kalantar-zadeh, *Chem. Commun.*, 2013, **49**, 6349-6351.
4. E. Eisenbarth, D. Velten and J. Breme, *Biomol. Eng.*, 2007, **24**, 27- 32.
5. J. Azadmanjiri, C. C. Berndt, J. Wang, A. Kapoor, V. K. Srivastava and C. Wen, *J. Mater. Chem. A*, 2014, **2**, 3695-3708.
6. G. R. Lee and J. A. Crayston, *J. Mater. Chem.*, 1991, **1**, 381-386.
7. S. Venkataraj, D. Severin, S. H. Mohamed, J. Ngaruiya, O. Kappertz and M. Wutting, *Thin Solid Films*, 2006, **502**, 228- 234.
8. H. Störmer, A. Weber, V. Fischer, E. Ivers-Tiffée and D. Gerthsen, *J. Eur. Ceram. Soc.*, 2009, **29**, 1743- 1753.
9. D. Bach, H. Störmer, R. Schneider, D. Gerthsen and J. Verbeeck, *Microsc. Microanal.*, 2006, **12**, 416- 423.
10. G. Ramírez, S. E. Rodil, S. Muhl, D. Turcio-Ortega, J. J. Olaya, M. Rivera, E. Camps and L. Escobar-Alarcón, *J. Non-Cryst. Solids*, 2010, **356**, 2714- 2721.
11. R. T. Tucker, M. D. Fleischauer, R. M. Shewchuk, A. E. Schoeller and M. J. Brett, *Mater. Sci. Eng. B*, 2011, **176**, 626- 632.
12. M. S. P. Francisco and Y. Gushikem, *J. Mater. Chem.*, 2002, **12**, 2552-2558.
13. I. Sieber, H. Hildebrand, A. Friedrich and P. Schmuki, *Electrochem. Commun.*, 2005, **7**, 97- 100.
14. Q. Lu, T. Hashimoto, P. Skeldon, G. E. Thompson, H. Habazaki and K. Shimizu, *Electrochem. Solid-State Lett.*, 2005, **8**, B17- B20.
15. R. A. Rani, A. S. Zoolfakar, J. Z. Ou, M. R. Field, M. Austin and K. Kalantar-zadeh, *Sens. Actuators B*, 2013, **176**, 149- 156.
16. K. Lee, Y. Yang, M. Yang and P. Schmuki, *Chem. Eur. J.*, 2012, **18**, 9521-9524
17. R. A. Rani, A. S. Zoolfakar, J. Subbiah, J. Z. Ou and K. Kalantar-zadeh, *Electrochem. Commun.*, 2014, **40**, 20-23
18. V. Surganov and A. Mozalev, *Extended Abstracts of the 40th International Society of Electrochemistry Meeting*, 1989, **2**, 81.
19. A. Mozalev, M. Sakairi, I. Saeki and H. Takahashi, *Electrochim. Acta*, 2003, **48**, 3155- 3170.
20. N. Tatarenko and A. Mozalev, *Solid-State Electron.*, 2001, **45**, 1009- 1016.
21. A. Mozalev, V. Khatko, C. Bittencourt, A. W. Hassel, G. Gorokh, E. Llobet and X. Correig, *Chem. Mater.*, 2008, **20**, 6482- 6493.
22. A. Mozalev, H. Habazaki and, J. Hubálek, *Electrochim. Acta* 2012, **82**, 90- 97.
23. A. Mozalev, M. Sakairi and H. Takahashi, *J. Electrochem. Soc.*, 2004, **151**, F257- F268.
24. S. H. Park, Y. H. Kim, T. G. Lee, H. K. Shon, H. M. Park and J. Y. Song, *Mater. Res. Bull.*, 2012, **47**, 3612- 3618.
25. H. Habazaki, T. Ogasawara, H. Konno, K. Shimizu, S. Nagata, P. Skeldon and G. E. Thompson, *Corros. Sci.*, 2007, **49**, 580- 593.
26. A. Mozalev, M. Sakairi, H. Takahashi, H. Habazaki and J. Hubálek, *Thins Solid Films*, 2014, **550**, 486- 494.
27. K. Nagahara, M. Sakairi, H. Takahashi, K. Matsumoto, K. Takayama and Y. Oda, *Electrochim. Acta*, 2007, **52**, 2134- 2145.
28. G. C. Wood, In *Oxides and Oxide Films*; Diggle, J. W. Eds.; Marcell Dekker: New York, 1987, pp. 41.
29. M. C. Biesinger, L. W. M. Laua, A. R. Gerson and R. St. C. Smart, *Appl. Surf. Sci.*, 2010, **257**, 887- 898.
30. NIST Standard Reference Database 20, Version 3.4 (web version), http://srdata.nist.gov/xps/.
31. J. F. Moulder, W. F. Stickle, P. E. Sobol and K. Bomben, In *Handbook of X-Ray Photoelectron Spectroscopy 2nd ed.*; J. Chastain Ed.; Perkin-Elmer Corporation, Eden Prairie: Minnesota, 1992; pp.167.
32. D. C. Bharti and S. W. Rhee, *Thin Solid Films*, 2013, **548**, 195- 201.
33. R. King, H. C. Patel, D. A. Gulino and B. J. Tatarchuk, *Thin Solid Films*, 1990, **192**, 351- 369.
34. N. S. McIntyre and T. C. Chan, In *Practical Surface Analysis*, D. Briggs and M. P. Seah, Ed.; vol. 1, Wiley: New York, 1990; p.501.
35. S. Z. Chu, M. Sakairi, I. Saeki and H. J. Takahashi, *J. Electrochem. Soc.*, 1999, **146**, 2876- 2885.
36. H. Habazaki, P. Skeldon, K. Shimizu, G. E. Thompson and G. C. Wood, *Corros. Sci.*, 1995, **37**, 1497.
37. M. Nagayama, K. Tamura and H. Takahashi, in *Proc. Intern. Cong. Metal Corrosion, Natl. Assoc. Corros. Eng.*, N. Sato, Ed., p. 175, Houston, Texas (1974)
38. I. A. Vrublevsky, A. I. Jagminas and K. V. Chernyakova, *Electrochem. Soc.*, 2013, **160 (6)**, C285- C290.
39. A. Mozalev, A. J. Smith, S. Borodin, A. Plihauka, A. W. Hassel, M. Sakairi and H. Takahashi, *Electrochim. Acta*, 2009, **54**, 935-945
40. N. Ramgir, N. Datta, M. Kaur, S. Kailasaganapathi, A. K. Debnath, D. K. Aswal and S. K. Gupta, *Colloids Surf., A* 2013, **439**, 101-116.
41. Z. Wang, Y. Hu, W. Wang, X. Zhang, B. Wang, H. Tien, Y. Wang, J. Guan and H. Gu, *Int. J. Hydrogen Energy*, 2012, **37**, 4526-4532.
42. K. K. Makhija, A. Ray, R. M. Patel, U. B. Trivedi and H. N. Kapse, *Bull. Mater. Sci.*, 2005, **28**, 9-17.
43. R. Calavia, A. Mozalev, R.M. Vázquez, I. Gràcia, C. Cané, R. Ionescu and E. Llobet, *Sens. Actuators B*, 2010, **149**, 352-361.
44. S. Mostafa, J. R. Croy, H. Heinrich, B. R. Cuenya, *Appl. Catal. A: Gen*, 2009, **366**, 353–362.
45. D.N. Suryawanshi, D.R. Patil and L.A. Patil, *Sens. Actuators B*, (2008), **134**, 579‑584.

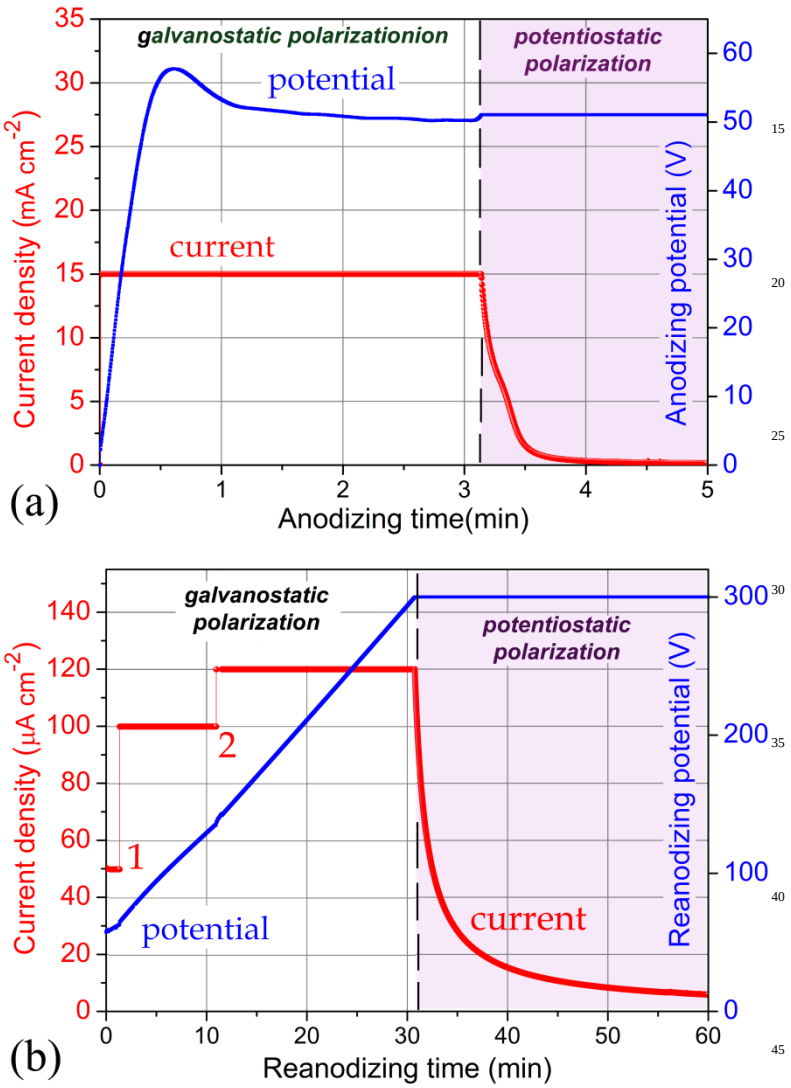

Fig. 1. The potential-time and current-time responses for (a) anodizing in 0.2 mol dm^{-3} $H_2C_2O_4$ electrolyte and (b) reanodizing in 0.1 mol dm^{-3} H_3PO_4 electrolyte of an Al(1μm)/Nb(300nm) bilayer (aluminum-on-niobium) sputter-deposited onto an oxidized Si wafer.

This journal is © The Royal Society of Chemistry [year]

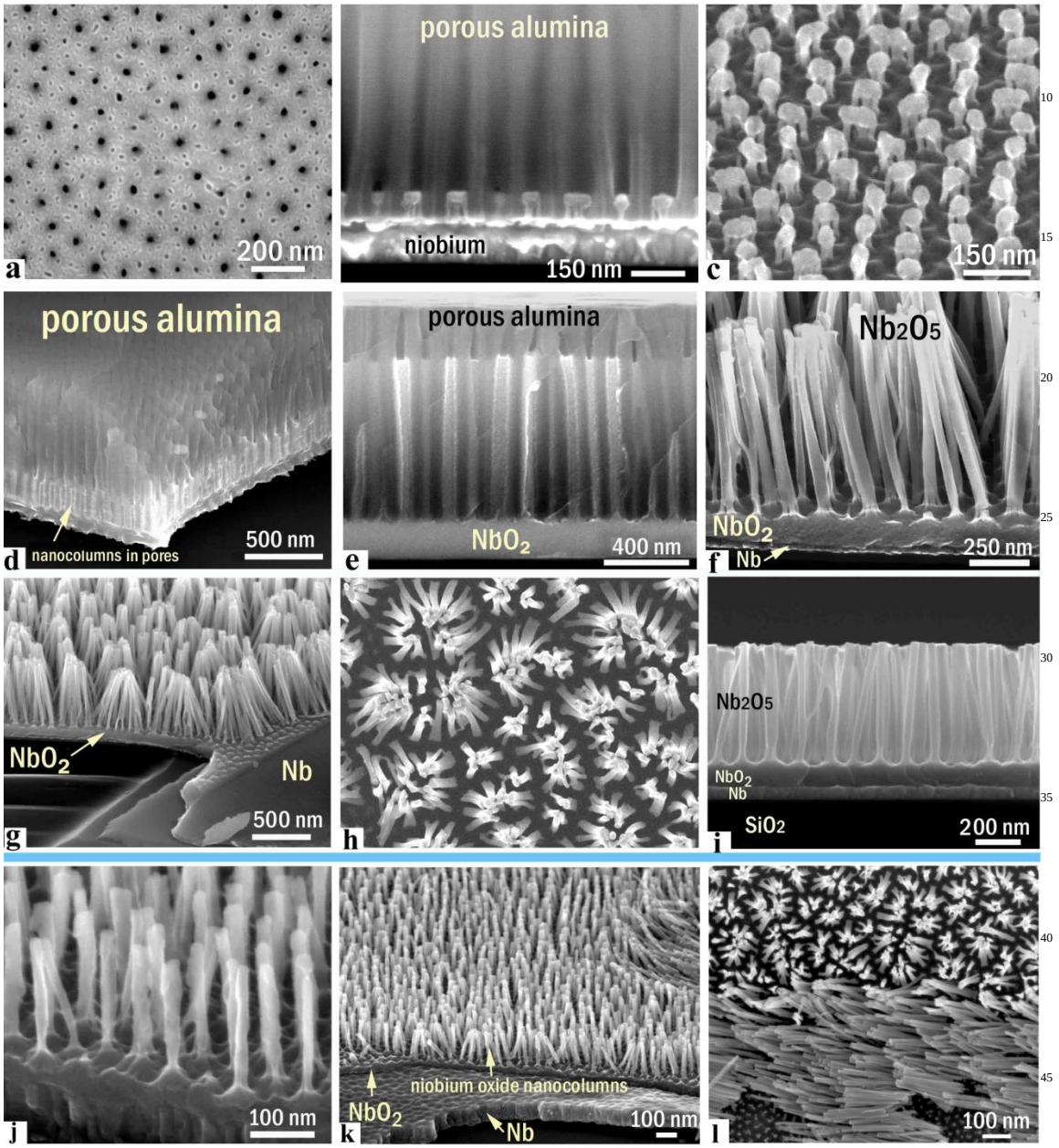

Fig. 2. SEM views of Al/Nb bilayers on SiO_2/Si substrates: (a-c) anodized at 52 V in 0.2 mol dm^{-3} $H_2C_2O_4$ and then reanodized in 0.1 mol dm^{-3} H_3PO_4 to (d-h) 450 V and (i) 300 V; (j-l) anodized at 26 V in 0.2 mol dm^{-3} H_2SO_4 and then reanodized to 150 V in 0.1 mol dm^{-3} H_3PO_4. The images shown in (c, f-l) were obtained after the alumina layer had been dissolved away ("alumina-free" samples).

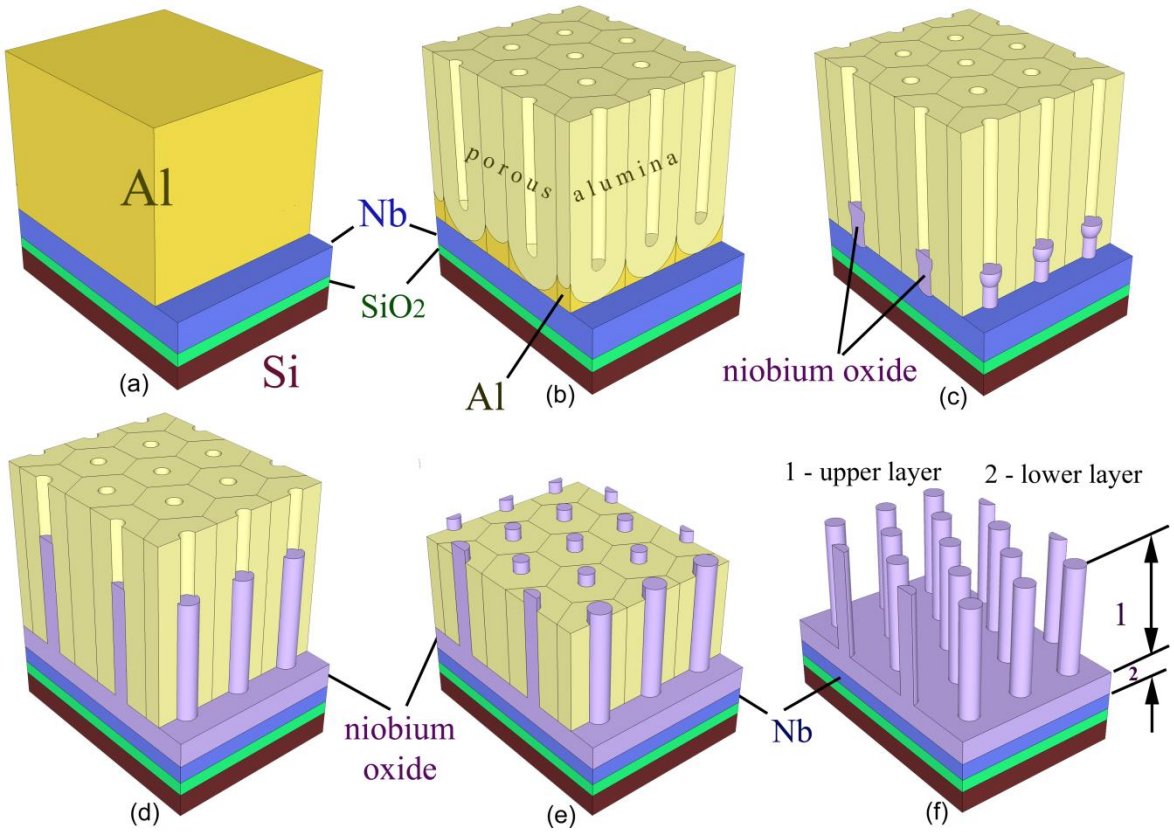

Fig. 3. The main phases of film formation process: (a) sputter-deposition of an Al/Nb bilayer on an SiO_2/Si substrate, (b) growth of a porous alumina film, (c) anodizing the Nb underlayer through the alumina nanopores, (d) growth of niobium oxide nanocolumns in the alumina pores, (e) partial dissolution of the alumina overlayer ("pore-free" sample), and (f) complete dissolution of the alumina overlayer

This journal is © The Royal Society of Chemistry [year]

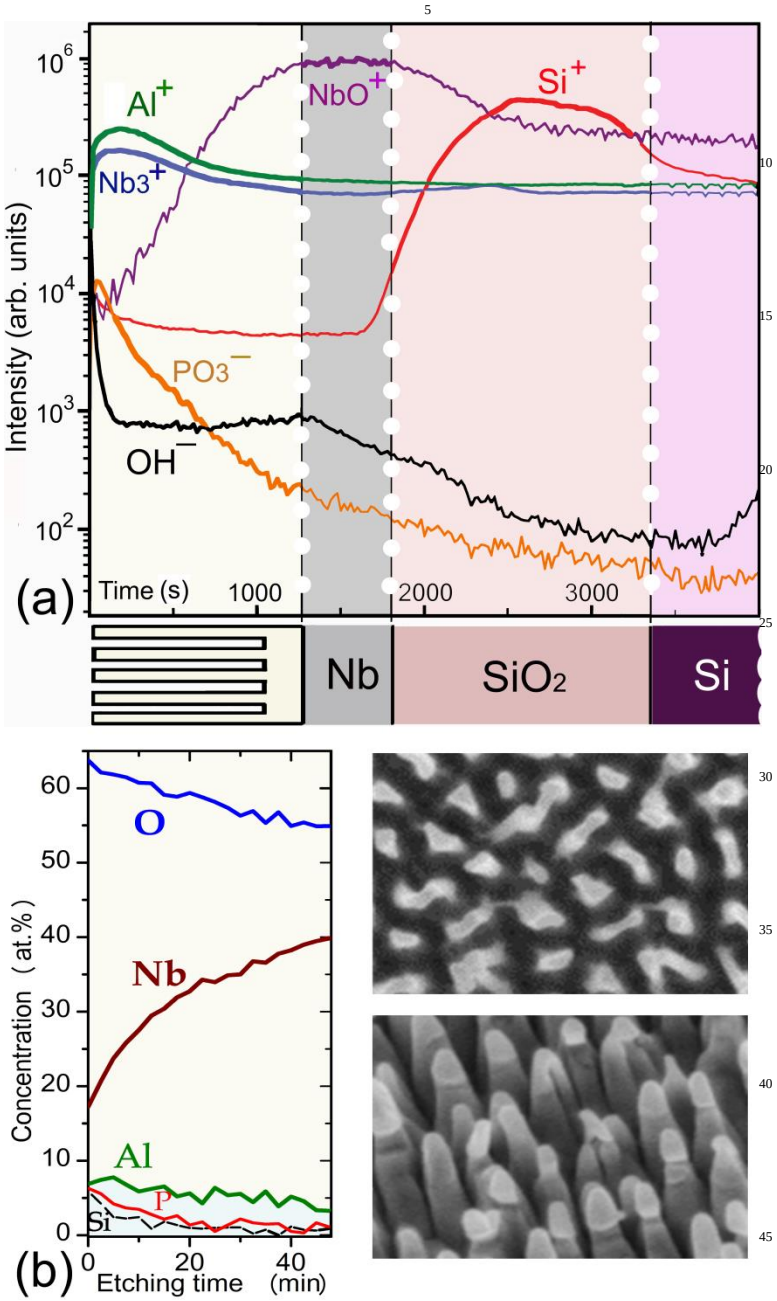

Fig. 4. (a) ToF-SIMS depth profiles and (b) XPS atomic concentration profiles for the alumina-free sample (as in Figure 2i). The SEM images show how the film surface changes after the Ar-ion sputtering.

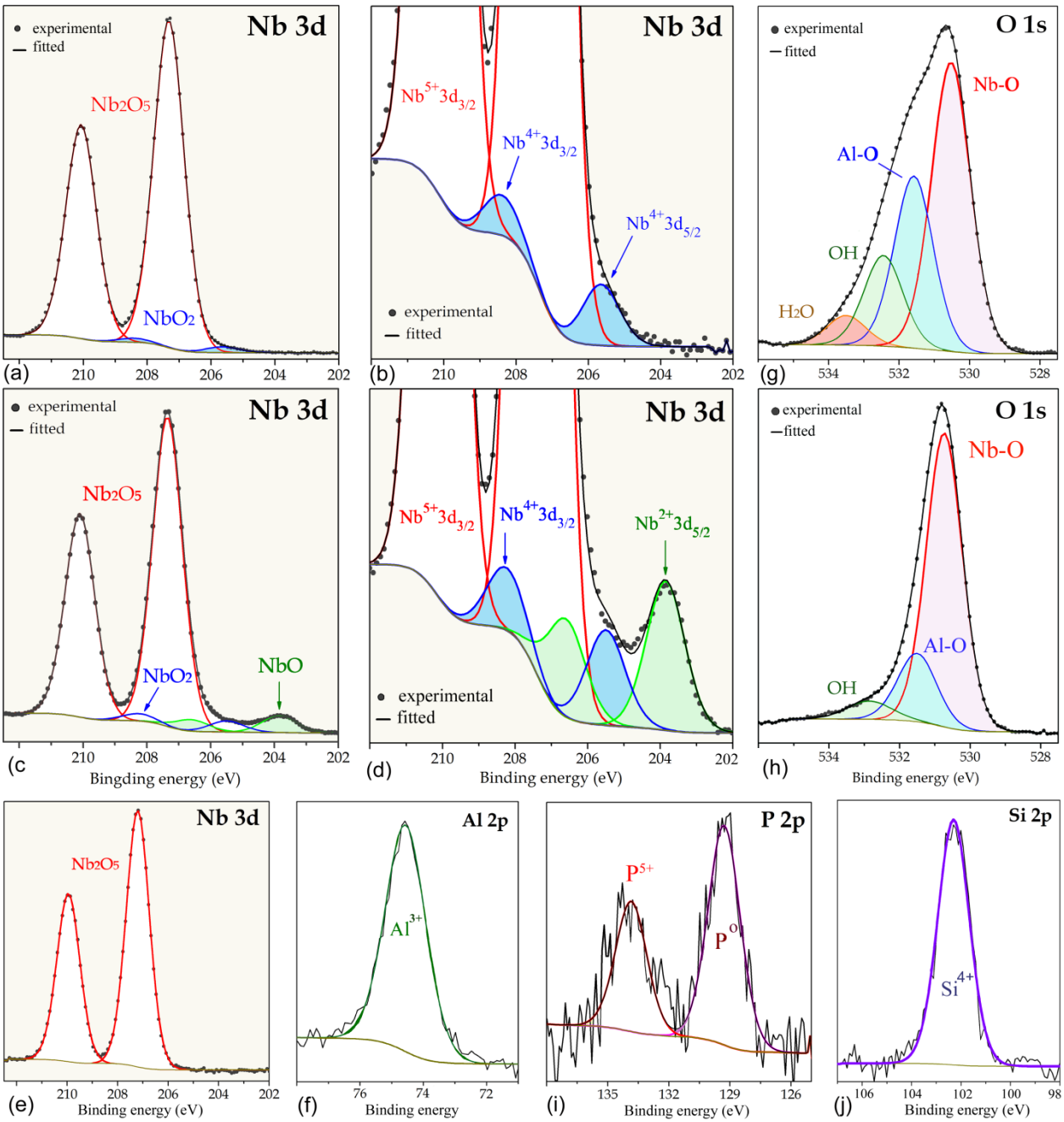

Fig. 5. Experimental and curve-fitted XPS spectra of (a,b) Nb 3d for the unsputtered alumina-free sample (as in Figure 2i), (c,d) Nb 3d for the unsputtered vacuum-annealed alumina-free sample, (e) Nb 3d for the unsputtered pore-free sample (as in Figure 3e), (f) Al 2p for the sputter-cleaned alumina-free sample, (g,h) O 1s for the unsputtered and Ar-ion sputtered alumina-free sample, respectively, (i) P 2p of the Ar-ion sputtered alumina-free sample, and (j) Si 2p for the sputter-cleaned alumina-free sample

This journal is © The Royal Society of Chemistry [year]

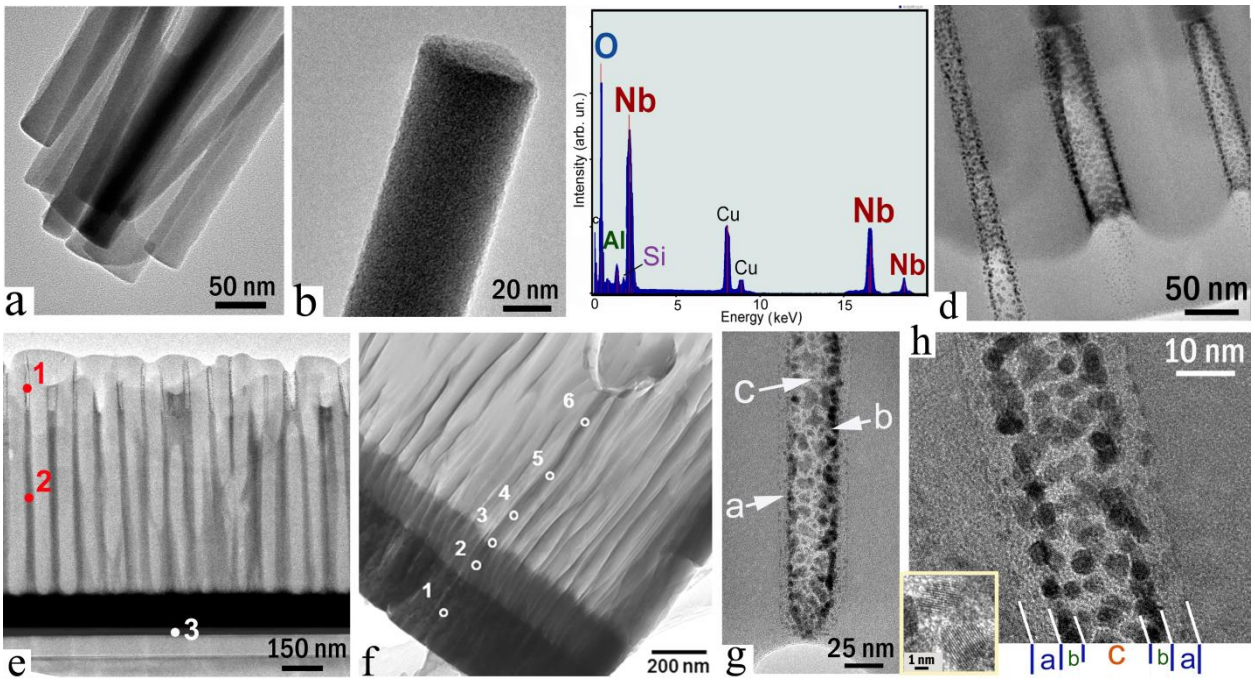

Fig. 6. (a,b) TEM images made of individual niobium oxide columns that had been scratched away from the alumina-free sample, (c) result of X-ray microanalysis of a single column, (d,e,g,h) TEM images of a FIB-made lamella of an Al/Nb bilayer sequentially anodized/reanodized at 52V/450V (the inset in (h) reveals atomic planes in the niobium oxide), (f) TEM image of the ultramicrotomed section of an Al/Nb bilayer anodized/reanodized at 52V/310V. The spots marked on the images are approximate positions of the electron probes used for EDX analysis

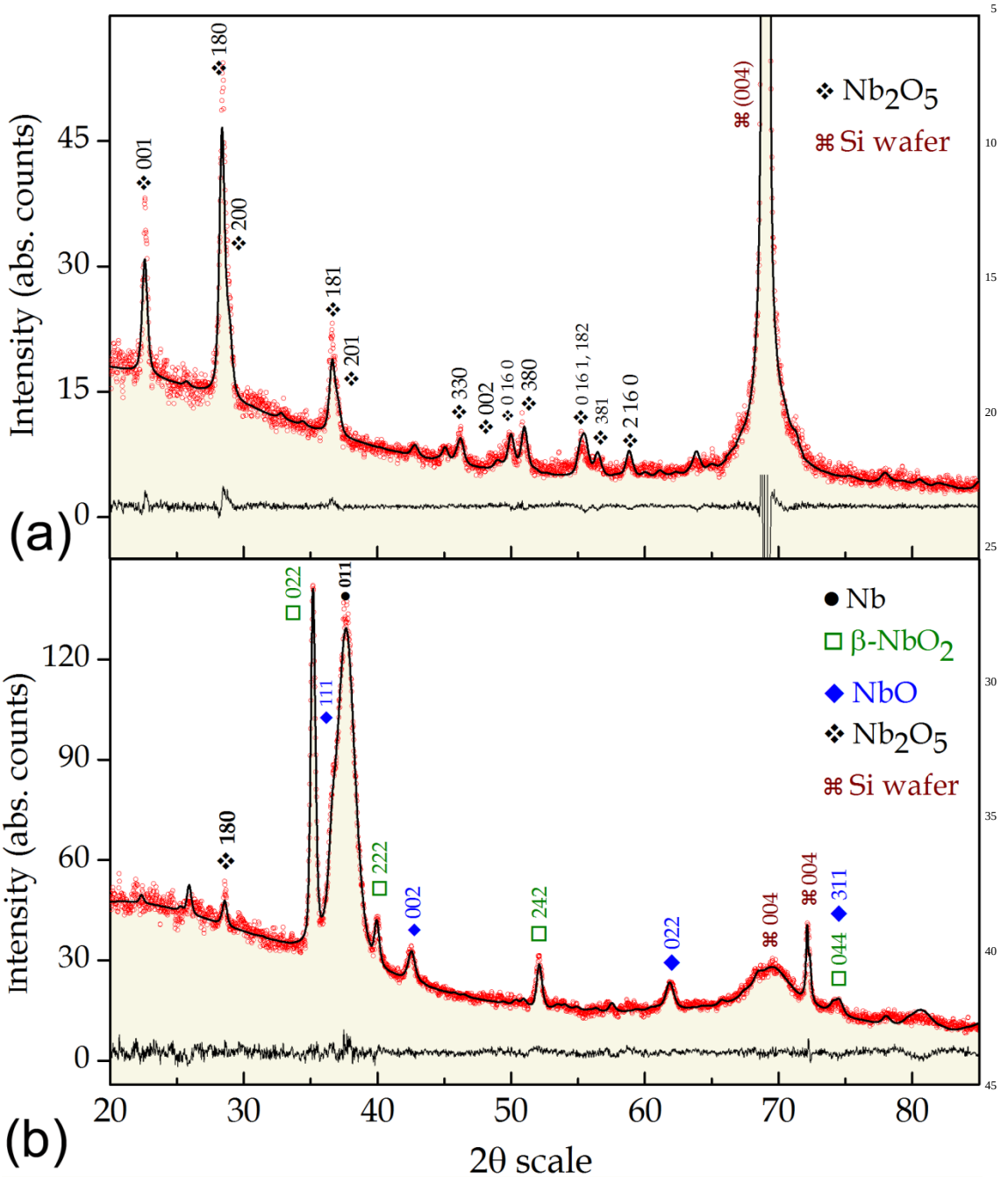

Fig. 7. X-ray diffractograms of the alumina-free sample (as in Figure 2i) annealed at 550°C in (a) air and (b) vacuum (heated over 2 hours at 10^{-5} Pa and then cooled down to room temperature).

This journal is © The Royal Society of Chemistry [year]

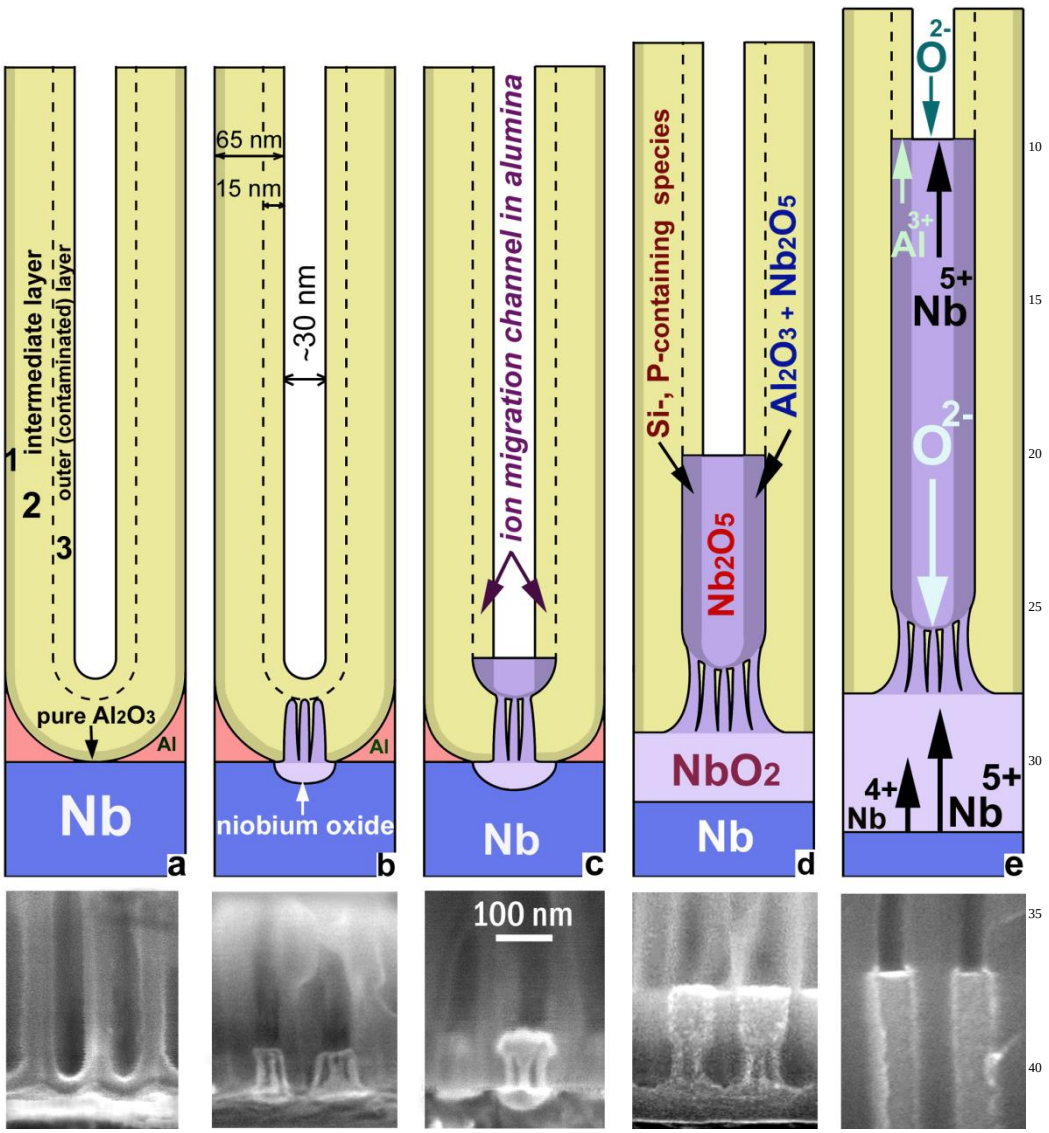

Fig. 8. Schematic model of oxide growth during the anodizing/reanodizing of an Al/Nb bilayer as in Figure 1: (a) porous anodizing of Al, (b) beginning of pore-assisted anodizing of Nb, (c) final stage of Nb anodizing, (d) beginning of Nb reanodizing, and (e) steady-state growth of niobium oxide during the reanodizing.

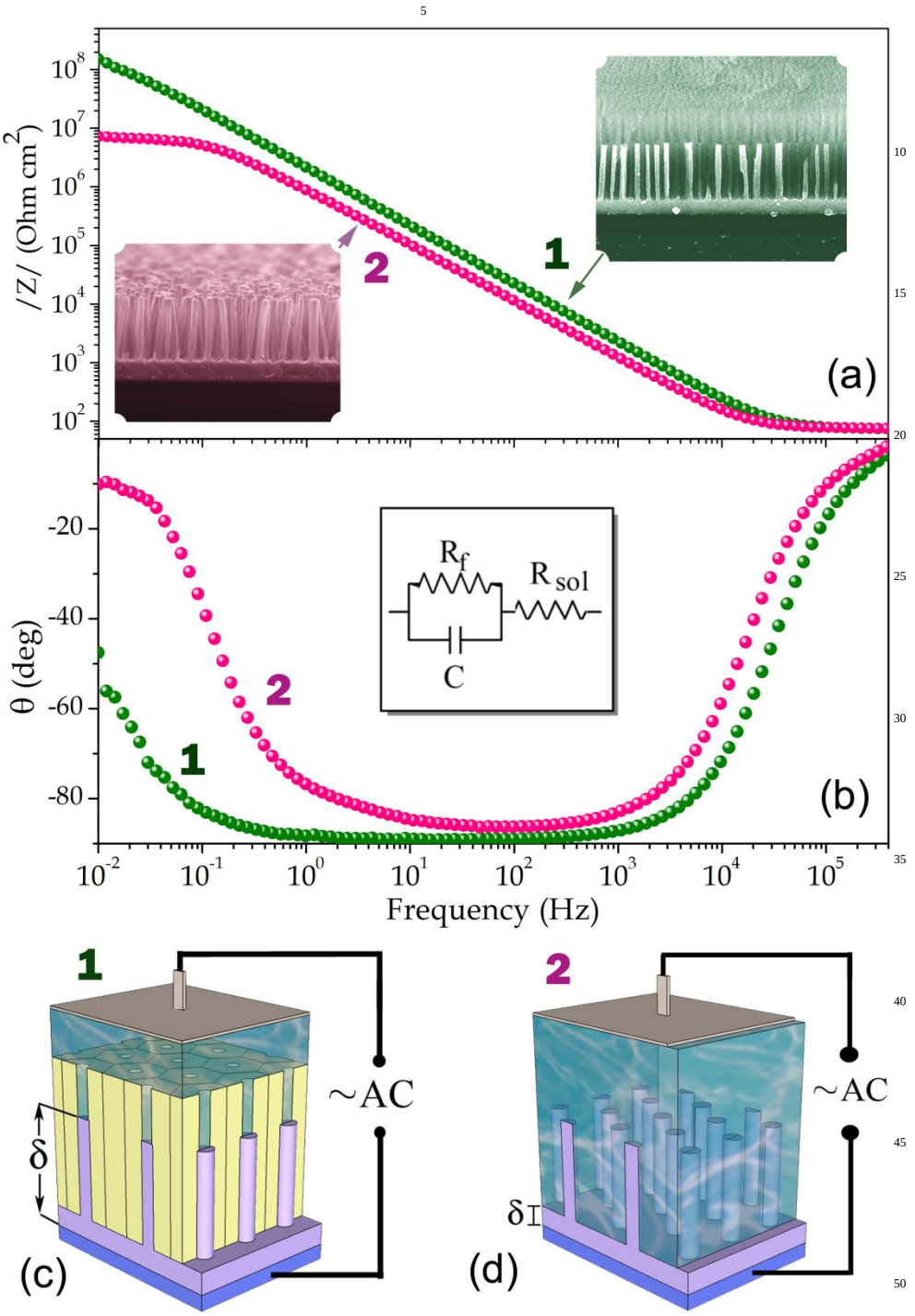

Fig. 9. Bode plots: (a) modulus of impedance /*Z*/ vs. frequency *f* and (b) phase angle θ vs. *f* for the as reanodized sample (curve 1) and the alumina-free sample (curve 2). The schematics show the setup for EIS measurements of the samples in solution.

This journal is © The Royal Society of Chemistry [year]

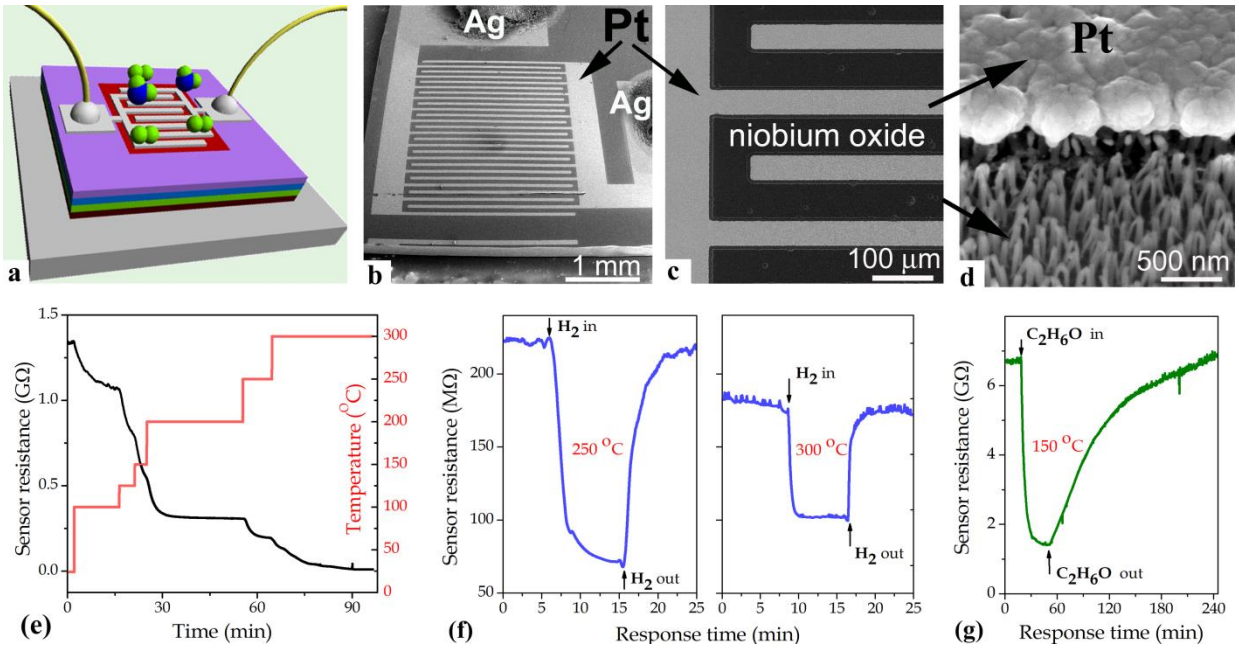

Fig. 10. (a) Schematic and (b-d) SEM images of a laboratory sensor employing the nanostructured niobium oxide film as active layer and the experimental sensor characteristics: (e) resistance-temperature response, (f) resistive response to hydrogen (H_2) 1000 ppm, and (g) resistive response to ethanol (C_2H_6O) 5 ppm.